CrossMark

ORIGINAL PAPER - PRODUCTION ENGINEERING

Fracture permeability under normal stress: a fully computational approach

Alexandre Lavrov[1]

Abstract Fractures contribute significantly to the overall permeability of naturally or hydraulically fractured reservoirs. In the cap rock, fractures may provide unwanted pathways for reservoir or stimulation fluids. Predicting fluid flow in naturally fractured rocks under production or fluid injection requires that permeability of a single, rough-walled fracture be well understood and accurately described as a function of the effective stress. The lack of information about the properties of fractures at depth calls for a numerical approach that would enable predicting the fracture permeability as a function of the effective normal stress. Such fully computational approach is developed in this study. The fracture deformation is calculated by solving the contact problem using the finite-element method. At each deformation step, the steady-state fluid flow in the fracture is computed in two orthogonal directions using the lubrication theory approximation, in order to evaluate the permeability and the hydraulic aperture of the fracture. The computational approach is tested on two examples: a 'brittle rock' (linear elastic) and a 'ductile rock' (linear elastic perfectly plastic). Both mechanical and hydraulic behaviours of the fracture under cyclic normal loading are found to be in qualitative agreement with the results obtained in a number of published experimental studies. The computational approach provides an insight into the actual mechanics of the fracture deformation under stress, and the effect of the latter on the permeability. In particular, hysteresis in the fracture roughness is obtained with the 'ductile rock', suggesting that (at least some) fractured rocks may retain 'memory' about their loading history imprinted in the fracture landscapes.

✉ Alexandre Lavrov
alexandre.lavrov@sintef.no

[1] SINTEF Petroleum Research, Trondheim, Norway

Introduction

The importance of fracture for fluid flow in subsurface rocks has been recognised in hydrology, geophysics, and reservoir engineering for at least three decades. In petroleum engineering, the naturally fractured reservoirs (carbonates, gas-bearing shale) stand out as a subject of their own, because of their remarkably different behaviour (Aguilera 1980). Naturally fractured reservoirs are those where fractures contribute crucially to storage and/or permeability. In reality, *all* rocks contain fractures, spanning in size from microcracks at grain scale to master joints extending for hundreds of metres (Twiss and Moores 2007).

Fracture permeability is a function of (i) the average opening of the fracture (which is often called the mechanical aperture); (ii) the roughness of the fracture faces caused by asperities. The roughness creates tortuous flow paths for the fluids (Brown 1987; Muralidharan et al. 2004). Hydraulic aperture of a fracture, w_h, is defined as the aperture of a smooth-walled conduit that has the same permeability as the real rough-walled fracture (Brown 1987; Zimmerman et al. 1991). The permeability of a fracture is thereby equal to $w_h^2 / 12$.

Note that the terms 'mechanical aperture', 'average aperture', and 'mean aperture' are used interchangeably throughout this manuscript, just as they are in modern rock mechanical and hydrogeological literature.

When compressive normal stresses in the rock are increased, a fracture closes, and its permeability declines. At the same time, the fracture stiffness increases since more contacts between the fracture faces are created, and

Springer

the area of the existing contacts increases (Chen et al. 2000; Pyrak-Nolte and Morris 2000). Similar effects, i.e. fracture closure and permeability reduction, are observed when the fluid pressure inside the fracture is reduced. Apart from direct reduction in the aperture, fracture closing increases the flow tortuosity since more asperities come into contact, and the flowing fluid has to go around them. This effectively increases the length of streamlines and pathlines, further reducing the hydraulic aperture of the fracture.

Unloading of a fracture, i.e. reduction in the normal stress, is usually accompanied with hysteresis in the fracture permeability: the fracture permeability is different during unloading from what it was at the same stress during loading (Gutierrez et al. 2000). Hysteresis of the fracture permeability under normal loading is a manifestation of a more general irreversibility of rock deformation that also includes, for example, the 'stress-memory' capacity of rocks (Becker et al. 2010; Lavrov 2005).

Depletion of oil and gas reservoirs is known to be accompanied with fracture closure, which is one of the reasons for notoriously low recovery factors in naturally fractured reservoirs (e.g. recovery factors down to 10–15 % in some fractured carbonates). A recent study suggests that stress-dependent fracture permeability can reduce the cumulative ten-year production from an unconventional gas field by 10 % (Aybar et al. 2014). Designing hydrocarbon production from and fluid injection into such fields requires a good grasp of the basic mechanisms affecting fracture behaviour during depletion and injection. It also calls for quantitative estimates of fracture permeability as a function of drawdown (reservoir pressure reduction).

It should be noted that very little information about fracture morphology (incl. roughness) and properties of the fracture network is available in practice when a field is developed. This information is usually gathered by interpreting image logs (acoustic or electric). Such logs show only traces of the fractures on the borehole wall. The resolution of the currently available equipment is not sufficient to quantify the fracture aperture, let alone provide information about fracture roughness. Under these circumstances, use of analogues, e.g. fractured outcrop rocks, for deriving fracture behaviour of fractures at depth becomes difficult, if possible at all, since fracture properties at depth can only be guessed.

The inaccessibility of fractures at depth and unavailability of information on their properties motivate the development of a computational approach that would allow an engineer to derive fracture properties such as stiffness and permeability from the limited information about the rock and fractures that is available. The first objective of this study was to demonstrate the viability of such approach for a fracture subject to normal stress.

Many empirical and semi-empirical fracture deformation laws have been proposed in the literature over the past 40 years. These laws are typically obtained for specific rocks. Each of such laws is therefore not particularly useful for other rocks. A number of empirical and semi-empirical laws governing fracture deformation under normal stress are discussed in (Gangi 1978; Malama and Kulatilake 2003). As pointed out in (Gangi 1978), the empirical and semi-empirical laws, albeit useful for matching the experimental data for a specific rock, provide no insight into the physical mechanisms of stress-dependent fracture permeability.

The limited validity and applicability of empirical and semi-empirical fracture deformation laws has motivated the development of numerical models of fracture deformation under normal stress. Most of these models are based on the approach of a 'bed of nails' advocated in (Gangi 1978). In that study, asperities were considered as a collection of cylinders deforming independently of each other. It was shown that 'nails' of different shapes could be used and could bring about the same fracture deformation law as the cylinders, provided that the length distribution of the 'nails' is adjusted accordingly. A similar approach was taken in (Brown and Scholz 1986) where the Hertzian model was used to describe the interaction between asperities in contact. Independent interaction of asperities in models of this kind is a crude approximation. Another drawback of these models is the need for their calibration in terms of micromechanical parameters that cannot be easily obtained from a direct rock mechanical test. Despite the above weaknesses, tuning the model parameters enabled a good approximation of the measured normal stress versus fracture closure curves in (Brown and Scholz 1986; Gangi 1978). The Hertzian model was used to describe contact interaction between asperities also in a number of subsequent studies, e.g. (Lespinasse and Sausse 2000). A simplified description of the contact interaction was employed also in the work of (Pyrak-Nolte and Morris 2000) and (Detwiler and Morris 2014) who modelled asperities as circular cylinders behaving elastically at any stress.

It should be noted that, even though the above-mentioned simplified treatments of fracture deformation do provide a valuable insight into the mechanics of fracture closure, it is difficult to establish a relationship between the parameters of such models and measurable rock properties. Modern finite-element codes offer a more accurate, and consistent, description of contact interactions, without the major simplifications used in the above earlier works. In addition, the hard contact model implemented, for example, in the finite-element package ABAQUS and used in this study involves only measurable, macroscale properties of the rock, such as the Young's modulus and the Poisson's

ratio, and is therefore more suitable for practical applications. Unlike its empirical and semi-empirical counterparts, the finite-element model of the contact problem allows one to study directly the effect of different factors, such as the rock plasticity, on the fracture deformation.

It should be noted that most of the experiments on fracture deformation and fracture permeability under stress have been performed on brittle, crystalline rocks such as granite, quartzite, and marble. Studies on rocks showing some degree of plasticity, e.g. shale, are rare. Experiments of (Gutierrez et al. 2000) performed on Kimmeridge shale revealed irreversible, hysteretic fracture deformation under cyclic normal load. The fracture had nonmatching rough walls in that study. As a result, it was not possible to completely close such fracture by applying normal load. Even at normal stresses on the order of or higher than the unconfined compressive strength of the shale, the fracture permeability was several orders of magnitude higher than the matrix permeability of the rock. In contrast, experiments performed on an artificial, smooth-walled fracture using another shale (Opalinus Clay) demonstrated that the permeability of such fracture could be reduced virtually down to the matrix permeability by applying a sufficiently large normal stress (Cuss et al. 2011). The above two studies demonstrate the essential role of asperities in governing the mechanical and hydraulic behaviours of fractures in a ductile rock. It should be noted that asperities also have a significant impact on particle transport. In particular, surface roughness gives rise to hydrodynamic dispersion during particle transport in fractures (Bauget and Fourar 2008; Cumbie and McKay 1999; Koyama et al. 2008; Nowamooz et al. 2013).

The role of plastic deformation in contact interactions between asperities was recognised and confirmed via SEM analyses already by (Brown and Scholz 1986). However, their plasticity model, being part of the Hertzian contact model, was severely oversimplified.

The objectives of this study, in addition to demonstrating the viability of the computational approach, were as follows: to look into the effect of rock ductility (plasticity) on fracture permeability under normal stress; to look into the effect that normal stress might have on the roughness-induced anisotropy of the fracture permeability, in a relatively brittle rock and in a relatively ductile rock.

Computational workflow

The numerical workflow used for deriving fracture permeability as a function of normal stress in this work is as follows:

1. Generate two fracture surfaces. This is done numerically in this study. Alternatively, profilometry can be performed on geological samples of a fractured rock.

2. Use the two landscapes obtained in (1) to make two rock blocks (prisms), with each of the two landscapes being a face on one of the prisms. The prisms are then placed so that the two rough sides face each other (Fig. 1).

3. Import the two rock blocks into a finite-element software.

4. Fix one block and apply a desired history of normal loading–unloading to the other block, under displacement control.

5. At each displacement step, export the distribution of the fracture aperture and construct an updated fracture aperture landscape.

6. For each exported distribution of aperture, perform fracture flow simulations to derive the fracture permeability (the hydraulic aperture).

Items 1, 2, and 3 in the above list are pre-processing. Item 5 is post-processing. Items 4 and 6 are the actual numerical simulations.

The recursive subdivision technique was used in this study to generate two fracture faces numerically (step 1 in the above list) (Fournier et al. 1982). Both fracture surfaces were generated using the same parameters, in particular the Hurst exponent (a parameter linked to the fractal dimension of the fracture surfaces) equal to 0.7, and had the same in-plane dimensions of 32 cm × 32 cm. The Hurst exponent is typically around 0.8 for natural fractures in rocks (Detwiler and Morris 2014). The in-plane grid spacing was equal to 1 cm; thus, the fracture plane had à 33 nodes in the x- and y-directions. The discretisation was thus quite coarse. However, as shown by (Schmittbuhl et al. 2008), viscous flow in a fracture is controlled by long wavelengths of the fracture aperture landscape, at least when the fracture is opened. Therefore, as a first approximation, a coarse model was deemed sufficient. Using a fine grid would induce a prohibitive computational cost for the FEM model of mechanical deformation since the mechanical model was 3D, while the flow model was effectively 2D. All numerical computations in the workflow were performed on a desktop computer in this study. The relatively coarse resolution is sufficient to demonstrate the viability of our fully computational approach. Finer grids can be used in future work.

It should be noted that the procedure described above and used for generating the fracture faces numerically in this study implies that fracture faces do not match at the beginning of the simulation. According to (Gangi 1978), this is a reasonable conjecture since, even in the case where the fracture faces could potentially be matching (e.g. freshly formed tensile fracture without shear displacement in hydraulic fracturing), the fracture will most likely be kept opened at some spots by gouge (small broken pieces

Fig. 1 Two rock blocks with the fracture between them
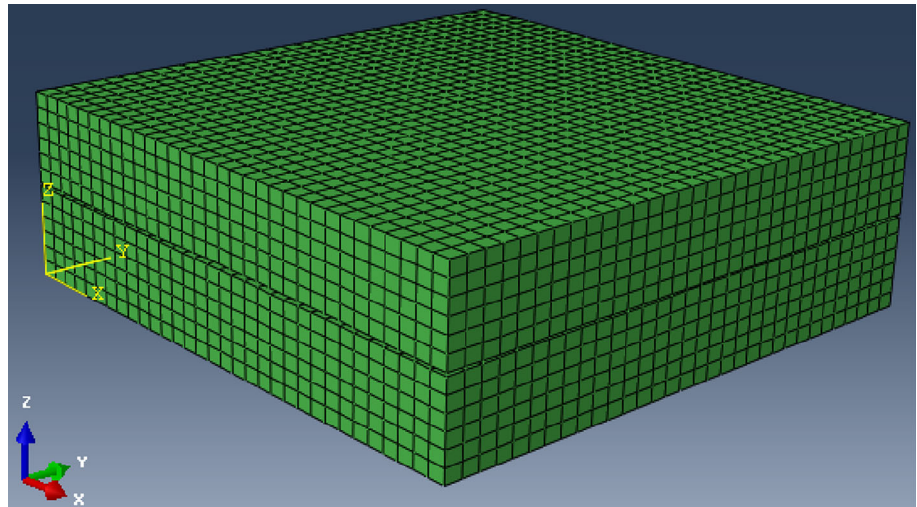
of rock dislodged from the fracture faces). The latter would play the role of asperities even in the rare cases where the fracture faces could match.

The grid spacing of 1 cm ensured that the lubrication theory approximation would hold in flow simulations (step 6 in the above list). It should be noted that, instead of numerical generation of the fracture landscape, a real landscape could be obtained from a real rock sample using, for example, mechanical profilometry (Lespinasse and Sausse 2000) or laser profilometry (MŁynarczuk 2010; Schmittbuhl et al. 2008).

A structured mesh of hexahedral elements was then generated in both blocks (step 2 in the above list). The two meshed blocks are shown in Fig. 1. The two blocks were then imported into a finite-element code (item 3 in the above list). ABAQUS was used in this study, but any other FEM code capable of handling contact problems could be used as well.

ABAQUS is a commercially available general-purpose finite-element code widely used for solving problems in solid mechanics. In this work, static stress analysis of fracture deformation under normal displacement was performed with ABAQUS. The following boundary conditions were applied on the bottom block: rollers at the bottom side ($z = 0$), the front side ($y = 0$), and the left-hand side ($x = 0$). See Fig. 1 for the coordinate system. For the top block, z-displacement was applied at the top side. The loading was thus displacement-controlled. The intention was to reproduce the boundary conditions of a laboratory test used to study fracture deformation and flow.

After the finite-element simulation of fracture deformation was completed, the reaction force on the top surface of the top block was extracted. From this force, the averaged applied stress was calculated at each displacement step. Furthermore, the distribution of the contact opening was exported for each displacement step. These data were

then used to construct an updated fracture aperture profile (step 5 in the above list).

For each updated fracture profile, a steady-state flow simulation was performed to assess the fracture permeability and the hydraulic aperture. To this end, the updated fracture profiles were imported into a fracture flow code, and a steady-state simulation of unidirectional flow of an incompressible Newtonian fluid was performed by applying a pressure gradient in the x-direction, i.e. between the sides $x = 0$ and $x = 32$ cm of the fracture. It should be noted that the fracture permeability is usually so much greater than the matrix permeability that matrix porosity and permeability were neglected in this study, and only flow inside the fracture was considered (with no matrix–fracture fluid exchange and no poroelastic effects in the matrix).

The fracture flow code solved the problem under the assumptions of the lubrication theory approximation. These assumptions are as follows (Zimmerman et al. 1991):

(i) the inertial effects are negligible, i.e. the Reynolds number is smaller than 1;

(ii) the velocity gradient in the fracture plane is much smaller than in the direction normal to fracture. This means in practice that the standard deviation of the aperture distribution is smaller than the largest wavelength of the aperture profile.

Under the above assumptions, the flow equation is given by (Brown 1987; Keller et al. 1999):

$$\frac{\partial}{\partial x}\left(w^3 \frac{\partial p}{\partial x}\right) + \frac{\partial}{\partial y}\left(w^3 \frac{\partial p}{\partial y}\right) = 0 \tag{1}$$

where p is the fluid pressure inside the fracture; w is the local fracture aperture; x and y are Cartesian coordinates in the fracture plane. Equation (1) was solved on a regular Cartesian grid using the finite-volume method described and benchmarked elsewhere (Lavrov 2014). It should be

noted that numerical modelling of this type has been used for the evaluation of fracture permeability in many previous studies, e.g. (Brown 1987; Koyama et al. 2008).

From the flow simulation (step 6 in the above list), the hydraulic fracture aperture was obtained as a function of the normal stress or displacement. Other outputs, at each loading step, included distributions of fluid pressure and velocity in the fracture plane, maximum and average (mechanical) aperture of the fracture.

The numerical road map laid out above was tested on two examples:

(a) a linear elastic rock ('brittle rock');
(b) an elastic perfectly plastic rock ('ductile rock').

The 'brittle rock' may serve as a model for a fracture in a brittle, hard, crystalline rock. The 'ductile rock' may serve as a model for a fracture in a soft, sedimentary rock showing significant plasticity, such as some shales.

Results

Brittle rock

The material properties of the rock are given in Table 1. The rock was linear elastic and might serve as analogue to a hard rock under stresses that do not exceed its yield point.

The two blocks were initially placed in such a way that the initial mechanical aperture (the average distance

Table 1 Material properties in the simulation of a "brittle" rock

Property	Value
Young's modulus (GPa)	5.0
Poisson's ratio	0.3

between the rough fracture faces) was equal to 2 mm. There were no contact spots between the fracture faces at the beginning of the simulation. The displacement of the top surface of the top block was then increased from 0 to 5 mm so as to close the fracture. Since the material was linear elastic, the deformation was reversible, and no loading–unloading cycles were therefore performed in this simulation.

The averaged stress at the top surface of the top block versus applied displacement is shown in Fig. 2 (solid line, diamond markers). The solid line in Fig. 2 is quite nonlinear even though the rock is linear elastic. The nonlinearity was due to the fracture progressively closing as the displacement increased. The number and area of the contact spots were increasing with displacement, making the fracture effectively stiffer. This behaviour is well known from laboratory tests, e.g. (Pyrak-Nolte and Morris 2000). The rate of stiffness increase depends on the rate of formation of new contacts as the fracture surfaces are pressed against each other.

The plot in Fig. 2 is qualitatively similar to the stress–displacement plots in (Koyama et al. 2008; Malama and Kulatilake 2003). The displacement values represented by the solid line in Fig. 2 contain both the deformation (closure) of the fracture and the deformation (compression) of the bulk rock. As mentioned in (Koyama et al. 2008), the rightmost part of the solid curve corresponds to the elastic deformation of the bulk rock and is therefore linear in this simulation. The linear component of the deformation is plotted as a dashed line with triangular markers in Fig. 2. We now follow the procedure described in (Koyama et al. 2008) to extract the fracture deformation curve from these simulation data. Shifting the solid line leftwards so that it now passes through the origin produces the dashed line with square markers in Fig. 2. Shifting the dashed straight line with triangular markers leftwards, so that it now passes

**Fig. 2** Stress versus displacement obtained in the simulation of a 'brittle' rock
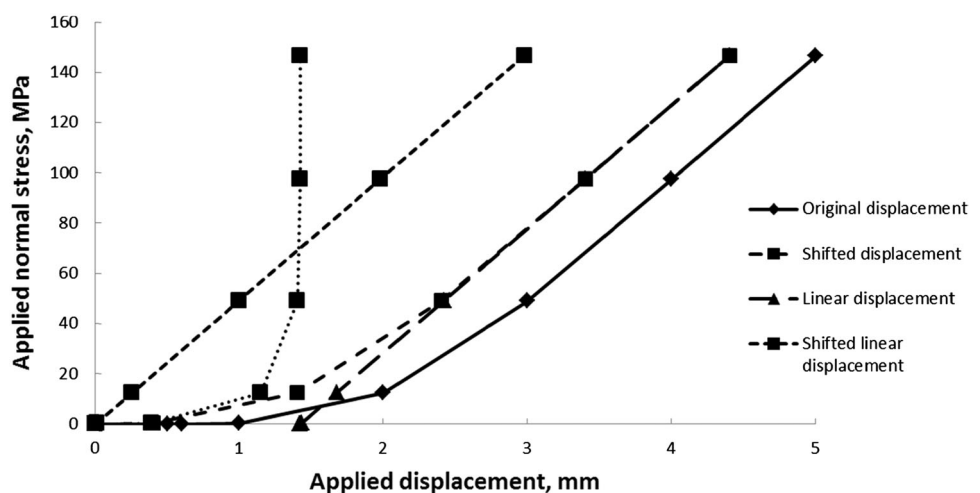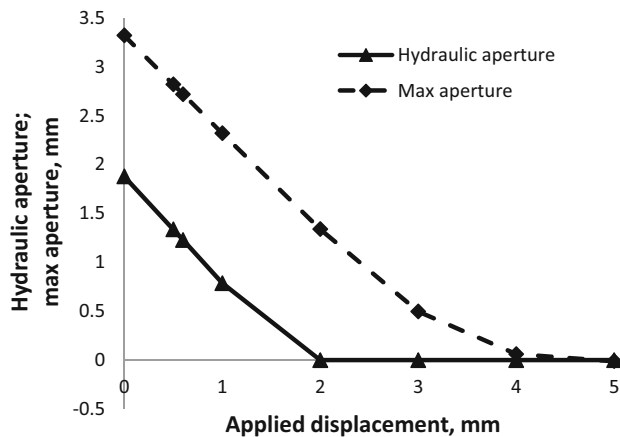
Fig. 3 Hydraulic and maximum apertures versus applied displacement obtained in the simulation of a 'brittle' rock. Hydraulic aperture obtained with for flow in x-direction

Fig. 4 Average aperture versus applied normal stress obtained in the simulation of a 'brittle' rock

through the origin, produces the other dashed line with square markers in Fig. 2. Subtracting one dashed line with square markers from the other produces the dotted line, which is the *fracture deformation* curve. Its shape is similar to the fracture deformation curve in (Koyama et al. 2008). All deformation of the bulk rock material has been removed from the displacement represented by the dotted curve. The dotted curve represents the pure fracture deformation.

The fracture deformation curve in Fig. 2 has a vertical asymptote at 1.4 mm which, according to (Koyama et al. 2008), signifies the mechanical aperture of the fracture (i.e. the mean aperture) at zero normal stress. It is the theoretical maximum of the relative normal displacement of the fracture faces that can be achieved by increasing the compressive stress on the fracture.

Analysis of the fracture aperture distributions at subsequent displacement steps has shown that the fracture faces first touched each other when the applied displacement became equal to 1.0 mm. The greatest value of the local fracture aperture as a function of the applied displacement is shown in Fig. 3 (dashed line). It is evident from Fig. 3 that the fracture became completely closed *mechanically* at the last loading step, i.e. at the applied displacement of 5 mm. The flow through the fracture in the x-direction ceased, however, already at the displacement of 2 mm, as the hydraulic aperture data suggest (solid curve in Fig. 3). Figure 4 illustrates the decay of the mechanical aperture (average distance between the fracture faces) as the stress increases. The shape of the curve in Fig. 4 resembles the respective plot obtained in a laboratory experiment on a granitic rock (Chen et al. 2000). The main qualitative difference between the curve in (Chen et al. 2000) and the curve in Fig. 4 is that zero aperture was not reached in the former. In the simulation, a zero aperture is eventually
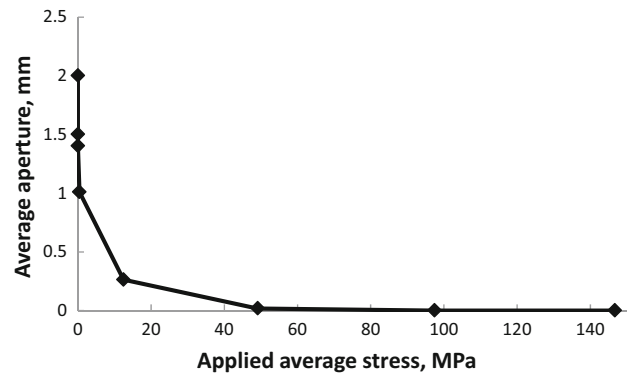
reached as the stress becomes sufficiently high. In a real test, the bulk rock may break or the loading capacity of the equipment may be exceeded before that happens.

Note that the hydraulic aperture shown in Fig. 3 was obtained when the pressure gradient was applied in the x-direction in the flow simulations, i.e. in the horizontal direction in Fig. 5. In the right-hand part of the fracture, a region of small aperture existed from the very beginning (blue region in Fig. 5a). As the loading proceeded, this region was closing first, until it completely blocked the flow in the x-direction (Fig. 5b). The flow was blocked because the fracture became completely closed along its right-hand side ($x = 0.32$ m), while a substantial percentage of the fracture area was still mechanically opened, i.e. had nonzero local aperture.

It should be noted that, if the fracture were larger, the fluid would probably be able to find a way around and to bypass the closed area. However, since all fractures, in practice, are finite, the percolating flow path would sooner or later cease to exist at some displacement value, and the hydraulic aperture would drop to zero. In the case of a real, rough-walled fracture with poorly matching faces and/or with gouge deposited inside the fracture, the fracture is likely to remain mechanically opened at some spots when the flow stops. The exact displacement at which the flow stops is expected to depend on the initial aperture, the fracture roughness distribution, and the in-plane dimensions of the fracture.
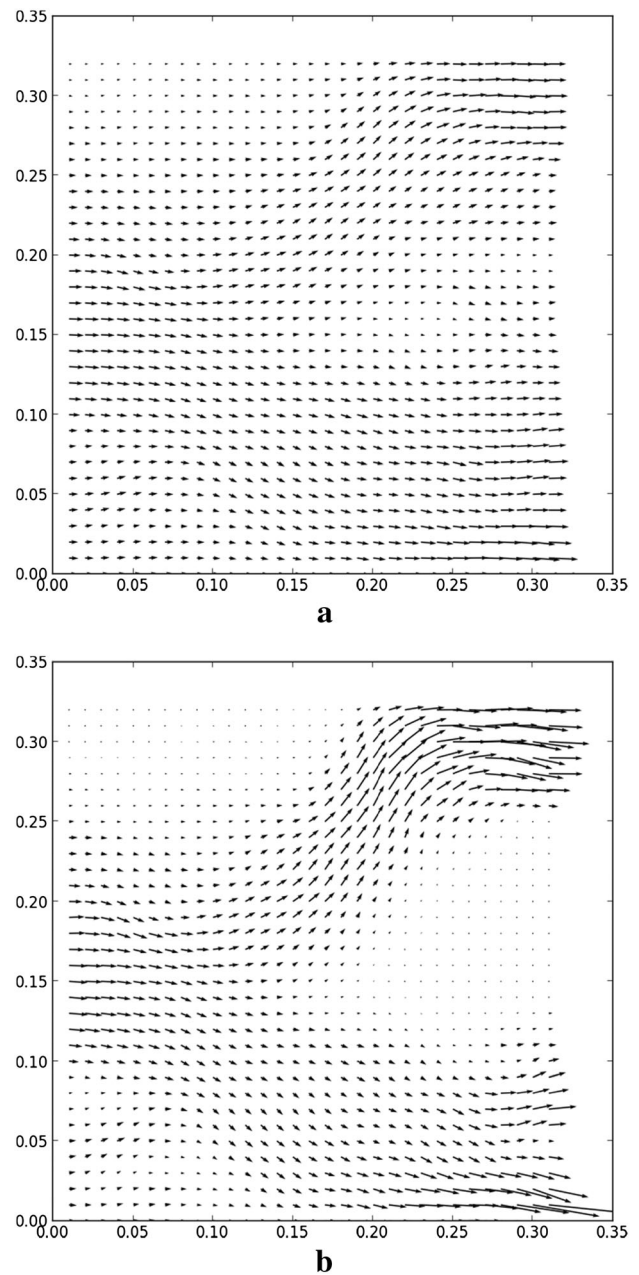
The difference between the concepts of the hydraulic and the mechanical aperture is evident in Fig. 5. Similar to isolated pores in porous media, open parts of the fracture in Fig. 5c create mechanical aperture, but do not contribute to the permeability of the fracture. Thus, the mean (i.e. mechanical) aperture is nonzero in Fig. 5c, whereas the hydraulic aperture is zero.

The effect of fracture closure on the fluid velocity and the fluid pressure distributions is evident in Figs. 6 and 7, respectively. The pressure gradient is quite uniform at the
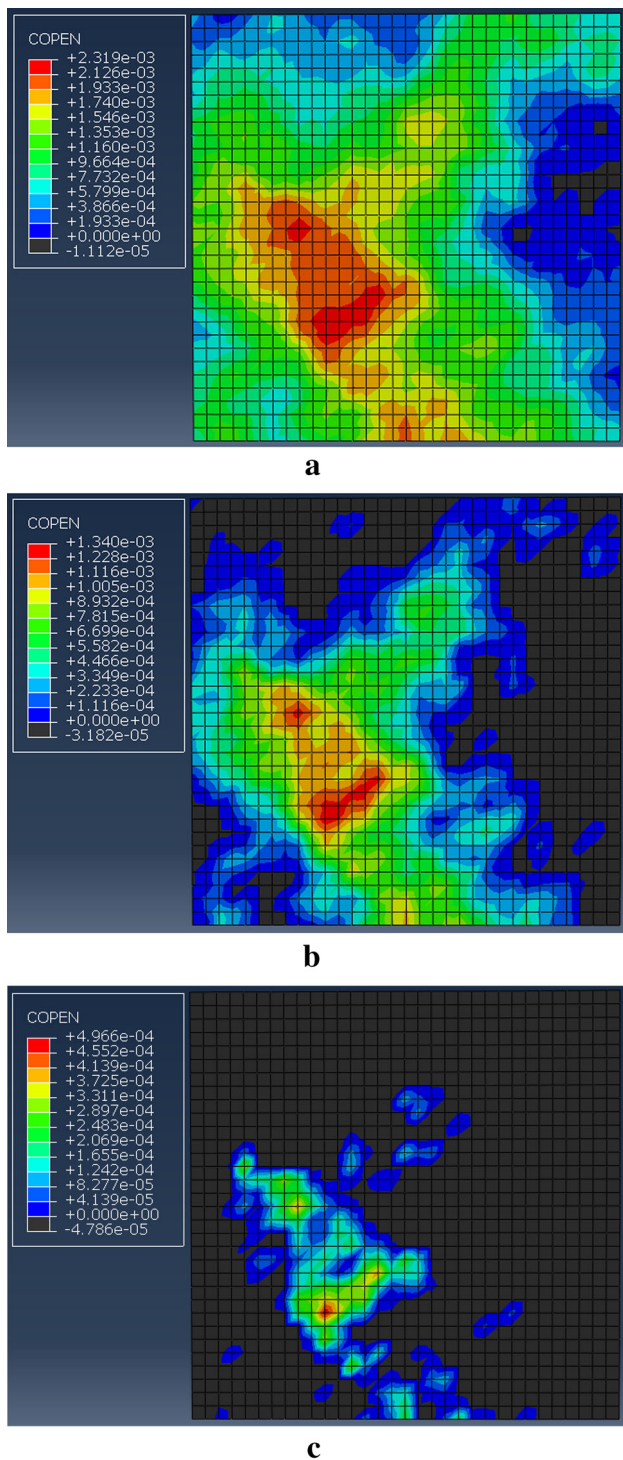
Fig. 5 Fracture aperture distributions at successive applied displacements in the simulation of a 'brittle' rock (unit of aperture in the legend: m). *Dark grey areas*: closed fracture (contact between the faces). **a** Displacement of 1.0 mm; **b** displacement of 2.0 mm; **c** displacement of 3.0 mm
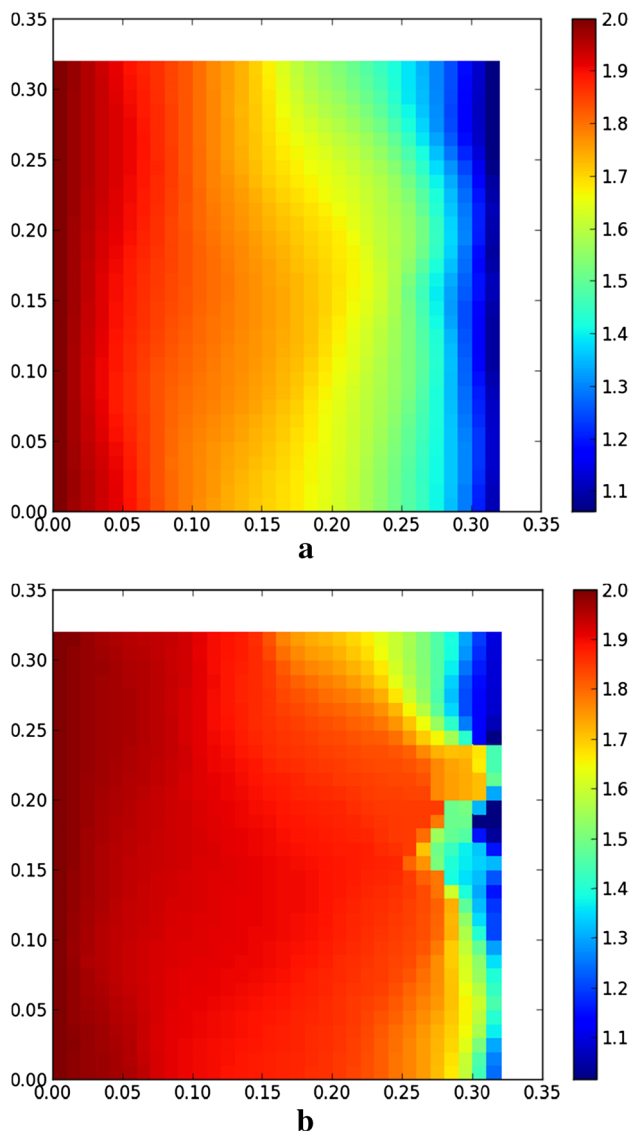

Fig. 6 Fluid velocity distributions at successive applied displacements in the simulation of a 'brittle' rock. Units along x- and y-axes are m. **a** Initial state, zero displacement of top surface; **b** displacement of 1.0 mm

the right-hand side of the fracture. As a result, most of the pressure drop occurs at the right-hand side in Fig. 7b. The fluid velocity field becomes increasingly tortuous as the loading proceeds (compare Fig. 6b to Fig. 6a).

Figure 8 shows the ratio of hydraulic to mechanical aperture, w_h/w, as a function of the mechanical aperture, w. As w increases, w_h/w asymptotically approaches 1, as expected since the effect of roughness decreases with w (the height of asperities becomes *relatively* small, compared to the steadily increasing fracture aperture).

beginning of the loading, when the fracture is wide open (Fig. 7a). As the loading proceeds, increasingly greater pressure drop is needed to flow through the constriction at

Fig. 7 Fluid pressure distributions at successive applied displacements in the simulation of a 'brittle' rock. Units along x- and y-axes are m. Pressure units in the legend are Pa. Pressure applied at the left-hand boundary is 2 Pa. Pressure applied at the right-hand boundary is 1 Pa. **a** Initial state, zero displacement of top surface; **b** displacement of 1.0 mm

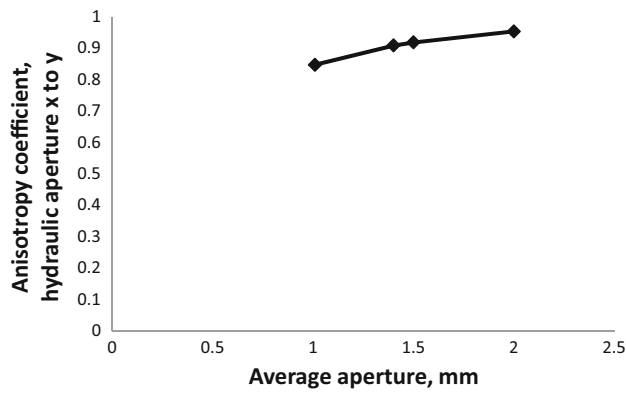**Fig. 8** Hydraulic-to-average-aperture ratio versus average aperture in the simulation of a 'brittle' rock
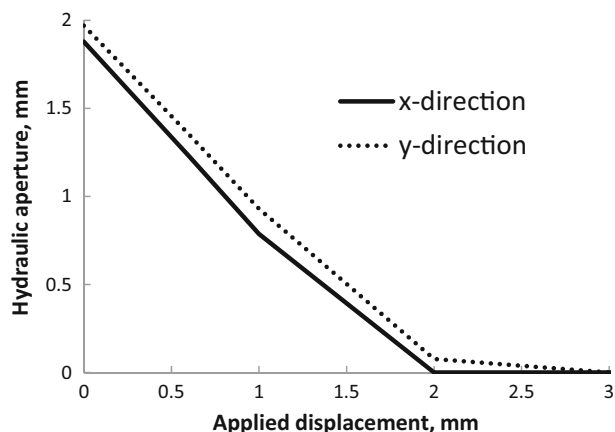
Fig. 9 Hydraulic aperture obtained with flow in x- or y-direction versus applied displacement in the simulation of a 'brittle' rock

It seems from the above exposition that the flow stoppage at displacement of 2 mm is controlled by the right-hand constriction in the fracture landscape. What if the flow were in the orthogonal direction? Would the results be different? In order to answer this question, flow simulations were repeated in the y-direction for all displacement steps. In turned out that the flow stopped at the next step, i.e. at 3-mm displacement, in this case. The results were in general quite similar to those obtained with the flow in the x-direction. The results obtained with the flow in the x- and y-directions are juxtaposed in Fig. 9. A striking similarity exists between the two curves in Fig. 9, despite the fact that

the numerical model is relatively small (33×33 nodes in the fracture plane), which might be expected to produce greater anisotropy.

As mentioned above, flow in the x-direction stops at displacement of 2 mm, while flow in the y-direction stops at displacement of 3 mm. A closer look at Fig. 5 reveals why and how this happens. It is evident from Fig. 5a that percolating clusters in both x- and y-directions do exist at displacement of 1 mm. From Fig. 5b, a percolating cluster only in the y-direction survives at displacement of 2 mm. From Fig. 9c, no percolating cluster can be found in the fracture. This is consistent with the difference in the evolution of w_h in the x- and y-directions in Fig. 9.

Figure 9 indicates that, although the anisotropy of the fracture permeability is quite small, it is present at all displacement steps. It is instructive to see how the permeability anisotropy evolves as the fracture closes. This is shown in Fig. 10 where the anisotropy coefficient is plotted as a function of the mechanical aperture. The permeability

Fig. 10 Anisotropy coefficient versus average aperture in the simulation of a 'brittle' rock

coefficient is here defined as the ratio of the hydraulic aperture obtained with the flow in the x-direction to the hydraulic aperture obtained with the flow in the y-direction. Figure 10 suggests that the permeability anisotropy is indeed quite small, and the fracture becomes more isotropic as it opens. In the limit of an infinitely wide fracture, the anisotropy coefficient would be equal to 1 for *any* fracture since the effect of the (finite) roughness becomes negligible as $w \rightarrow \infty$.

To conclude the elastic case, aperture histograms are presented in Fig. 11 for increasing displacements. The distribution of the aperture changes shape after the fracture faces come into contact. Contact spots emerge as a peak at the leftmost bin in Fig. 11c. Concurrently, the distribution acquires a 'fat tail' in Fig. 11c.

Ductile rock

The material properties used in the simulation of a 'ductile rock' are given in Table 2. The rock is linear elastic perfectly plastic and represents a ductile rock. As evident from Table 2, the elastic properties of the ductile rock were chosen equal to those of the brittle rock (see Table 1). This was done in order to single out the effect of rock plasticity on fracture behaviour. Thus, the two cases (ductile vs. brittle) differ only with regard to the plastic behaviour, while the elastic properties are identical. In reality, a 'typical' ductile rock would have elastic moduli lower than a 'typical' brittle rock.

Similarly to the elastic rock, the two rock blocks were initially placed in such way that the initial mechanical aperture was equal to 2 mm. There were no contact spots between the fracture faces at the beginning of the simulation. The displacement of the top surface of the top block was then increased from 0 to 5 mm. After the maximum displacement value of 5 mm had been reached, the applied displacement was decreased through the same steps from
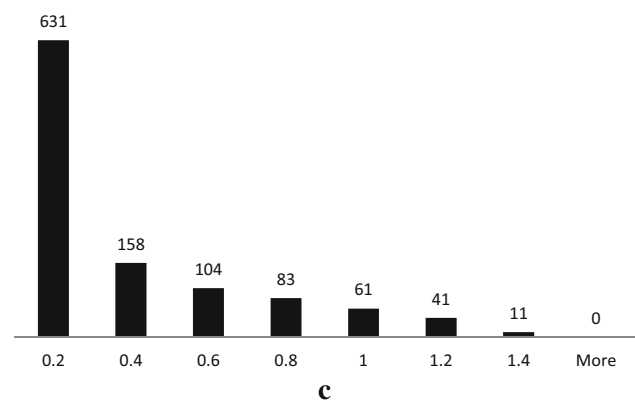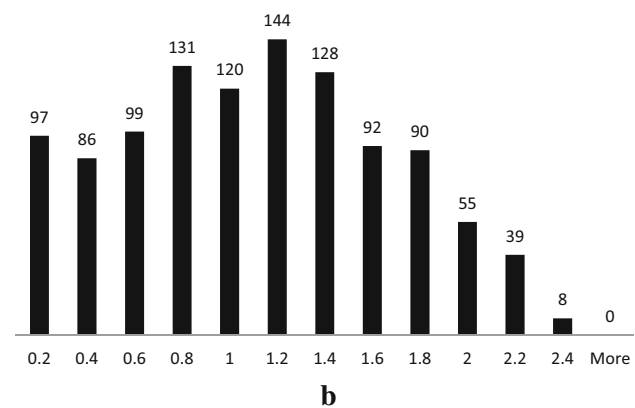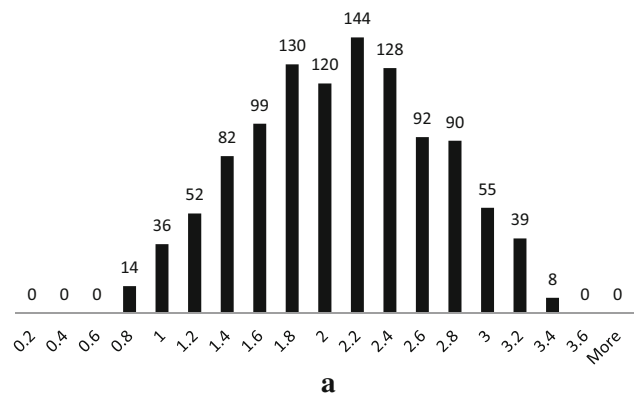
Fig. 11 Histograms of mechanical aperture (mm) at successive applied displacements in the simulation of a 'brittle' rock. **a** Initial state, zero displacement of top surface; **b** displacement of 1.0 mm; **c** displacement of 2.0 mm

Table 2 Material properties in the simulation with linear elastic perfectly plastic rock

Property	Value
Young's modulus (GPa)	5.0
Poisson's ratio	0.3
Cohesion (MPa)	5.0
Angle of internal friction (°)	30
Angle of dilatancy (°)	25

5 mm to 0. After that, a second loading cycle was performed: the displacement was again increased, retracing the same steps from 0 to 5 mm.

Averaged stress at the top surface of the top block versus applied displacement is shown in Fig. 12. The curve in Fig. 12 is nonlinear and has a significantly different shape than the respective curve for an elastic rock (Fig. 2, solid line). Namely, the curve is S-shaped during loading of the ductile rock. The nonlinear part at the beginning of the loading in Fig. 12 is caused by the same mechanism as the nonlinearity in the case of the elastic rock, i.e. an increase in the contact area. The nonlinear part at the end of the loading (rightmost part of the S-shaped curve in Fig. 12) is caused by plastic yield at contact points. Plastic yield leads to the flattening of the fracture faces by the end of the load increase. As a result, the aperture of the fracture is smaller and more evenly distributed than at the end of the loading of the elastic model. The hysteresis caused by plastic deformation at the fracture faces is evident in the evolution of the hydraulic aperture (Fig. 13). The evolution of w_h
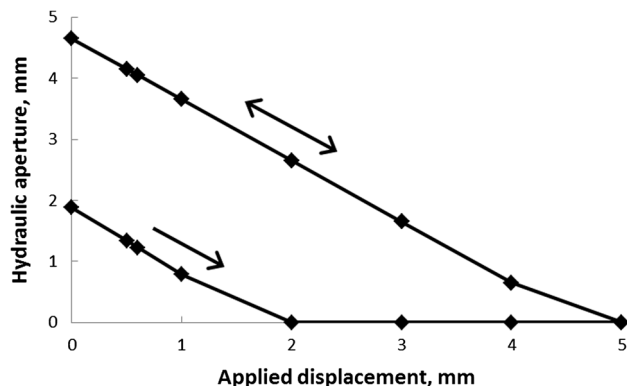
during loading resembles that in the elastic rock (cf. Fig. 3). However, whereas the same curve would be traced by an elastic rock during unloading as during loading, plastic deformation leads to a hysteretic loop in Fig. 13. The unloading branch is reversible. In addition, the unloading branch is linear, apart from a slight nonlinearity at the rightmost end (at the very beginning of unloading). The latter is caused by an elastic rebound of the fracture faces. After that, the two fracture faces become completely separated, and the increase in the aperture follows the displacement applied at the top side of the top block. Irreversible, plastic deformation of asperities experienced during compression in the first cycle results in the hydraulic aperture being virtually equal to the average (i.e. mechanical) aperture during subsequent unloading and reloading. This is evident in Fig. 14 (red curve).

The hysteresis evident in Figs. 13 and 14 results in different relationships between w_h and w at the initial loading and during subsequent unloading–reloading. During the initial fracture closing, the relationship between w_h and w is similar to that of an elastic rock. During unloading, the fracture surfaces are quite smooth because of the plastic deformation induced in the preceding loading. In subsequent loading cycles, the asperities do not cause so much flow tortuosity as they did in the original fracture, prior to the first loading cycle. Thus, repeated normal loading/unloading of a ductile rock reduces the permeability anisotropy of a fracture.

In addition to affecting the value of the hydraulic aperture, the repeated loading also affects the anisotropy of the fracture permeability. It is evident from Fig. 14 that the fracture was slightly anisotropic during the initial loading, just as its elastic counterpart was. During unloading and subsequent reloading, the fracture opened for flow, and its permeability was virtually identical in the x- and y-directions since the asperities were smoothed out by plastic
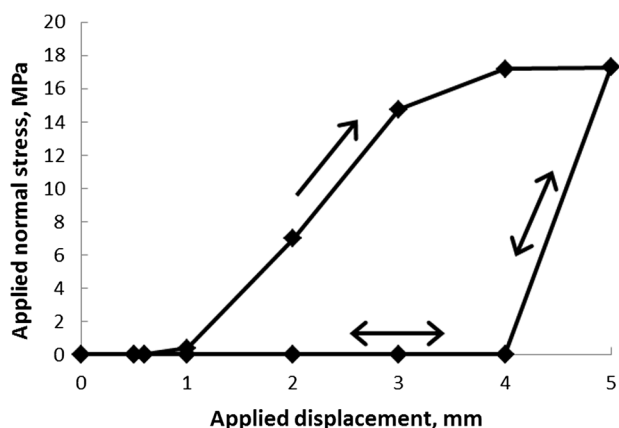

Fig. 12 Stress versus applied displacement in the simulation of a 'ductile' rock

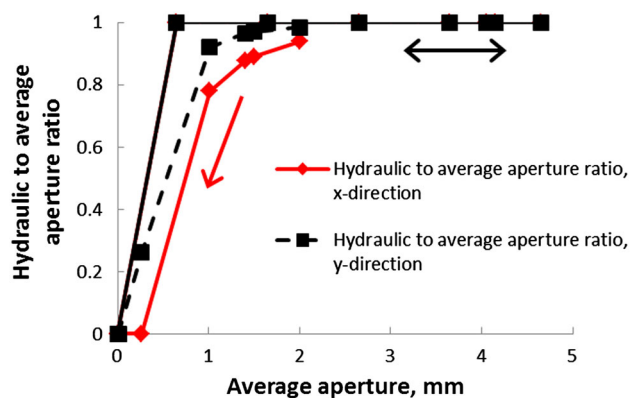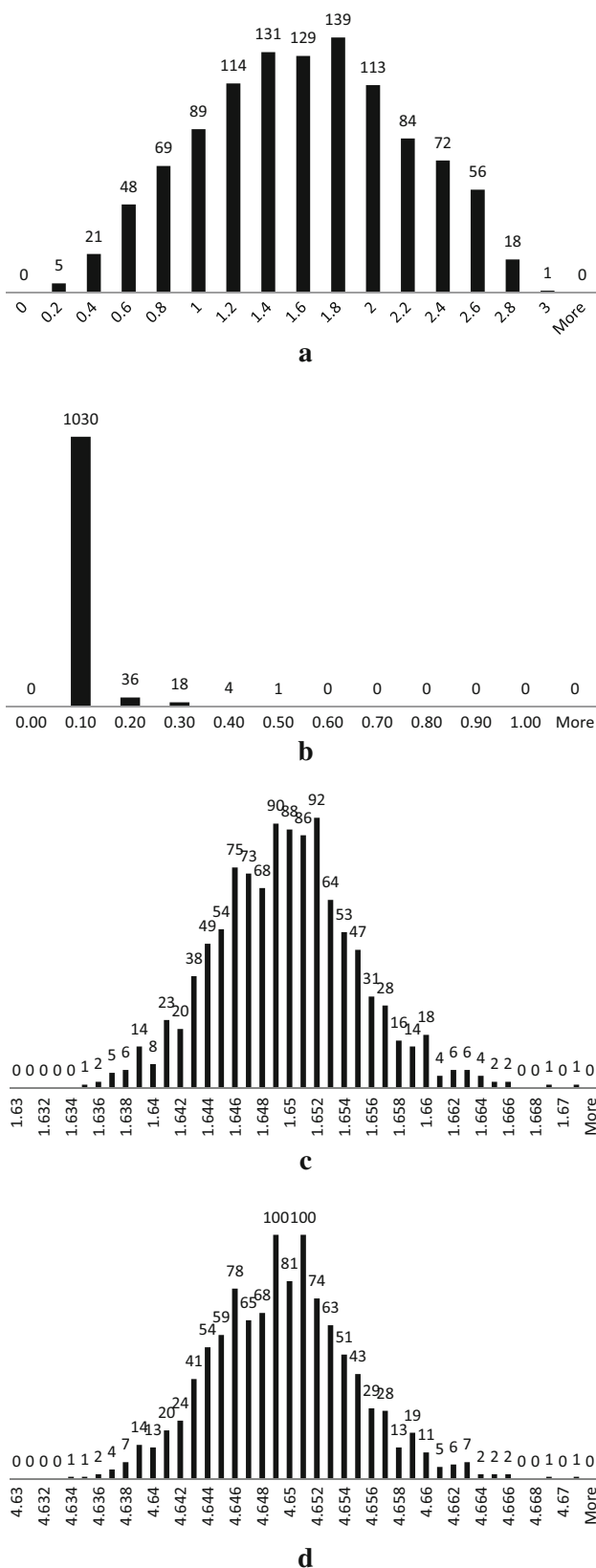Fig. 13 Hydraulic aperture versus applied displacement in the simulation of a 'ductile' rock

Fig. 14 Hydraulic-to-average-aperture ratio (flow in x- or y-direction) versus average (i.e. mechanical) aperture in the simulation of a 'ductile' rock

Fig. 15 Histograms of mechanical aperture (mm) at successive applied displacements in the simulation of a 'ductile' rock. **a** Displacement of 1.0 mm, loading (first cycle); **b** displacement of 3.0 mm, loading (first cycle); **c** displacement of 3.0 mm, unloading (first cycle); **d** zero displacement, end of unloading from the first cycle

deformation, and their impact on the flow tortuosity was thereby significantly reduced.

To conclude the ductile case, aperture histograms are presented in Fig. 15 for successive loading and unloading steps in the first cycle. Note that the initial distribution, prior to the first cycle, is identical to the brittle case and is shown in Fig. 11a. After the fracture faces come into contact, the distribution rapidly changes shape acquiring a fat tail in Fig. 15b, just as it did in the brittle rock. During unloading, an elastic rebound occurs, and the distribution becomes quite close to normal in Fig. 15c. The distribution of the aperture in the fracture that experienced plastic deformation is much narrower than it was in the original fracture (notice the scale of the horizontal axis in Fig. 15b, c). Subsequent parting of the faces of the already opened fracture shifts the distribution towards higher apertures without altering its shape (Fig. 15d).

Discussion

Hysteresis in the fracture permeability versus normal stress exhibited by the ductile rock suggests that caution should be exercised when transferring the results of laboratory measurements of the fracture permeability under stress onto in situ (reservoir) conditions. The rock could have been subject to a complex loading history in situ. Performing a single loading in the laboratory with an uncomplicated stress path is therefore likely to produce the fracture permeability figures that are not very representative for an in situ fracture.

Simulations suggest that there is no direct proportionality between the mechanical and the hydraulic aperture, even if the rock were perfectly elastic. Moreover, there might be a nonzero mechanical aperture below which there is no flow, i.e. below which the hydraulic aperture is zero. This is evident in Fig. 8.

The results presented in Fig. 8 are inconsistent with the empirical law of (Barton et al. 1985) which suggests that the ratio w_h/w should linearly increase with w:

$$\frac{w_h}{w} = \frac{w}{JRC^{2.5}} \tag{2}$$

where JRC is the joint roughness coefficient of the fracture surfaces. Earlier, (Chen et al. 2000) pointed out that Barton's formula was inconsistent with their experimental results. In

the case of our Fig. 8, the inconsistency with Eq. (2) is mainly in the existence of a threshold value of w below which there is no flow in our simulation. This might be the effect of finite fracture dimensions. However, even in a very large fracture, some isolated spots might remain opened after the flow is blocked as the fracture closes, thereby creating some nonzero, 'residual' mechanical aperture (similar to isolated pores creating porosity but not contributing to permeability in porous media). Therefore, the existence of a threshold value of w seems plausible albeit contradicting Eq. (2). This is also consistent with the discussion of flow in fractures of correlated versus uncorrelated landscapes in (Pyrak-Nolte and Morris 2000). In a fracture having a correlated aperture distribution (or, more precisely, when the correlation radius is the same order of magnitude as the in-plane fracture dimensions), the fluid flow is dominated by few preferential flow paths similar to those appearing in Fig. 6b. When these channels are closed during fracture deformation, the flow rate will drop to zero. On the other hand, in the case of uncorrelated landscapes (or, more precisely, in the case of a fracture with large in-plane dimensions compared to the correlation radius), asperities are distributed evenly across the fracture, and therefore, multiple flow paths are available even at large normal displacements.

Different behaviour of the fracture permeability in the first versus subsequent loading cycles in the ductile rock suggests that different fracture permeability closure laws might be applicable for mature fractures and fresh (newly created) fractures. The hysteresis in the mechanical behaviour of a fracture and in the fracture permeability under cyclic normal loading is known from experiments. An example is provided in (Gangi 1978) where it was attributed to the breakage of asperities in the first cycle. In our model of the 'ductile rock', the asperities irreversibly deform rather than break. It should be noted that irreversible (hysteretic) behaviour of fracture permeability was observed also in experiments on brittle rocks, e.g. (Scholz and Hickman 1983).

Experiments suggest that, in some cases, plasticity at contacts may contribute significantly to fracture permeability reduction at elevated normal stresses. This is corroborated, for instance, by digital strain imaging of a fracture formed at the interface between cement and rock (Walsh et al. 2012). In the latter experiment, plastic deformation was observed in the amorphous silica regions and regions depleted of Portlandite cement adjacent to the fracture faces. These chemical alterations were induced by exposure to CO_2. As a result, the reduction in the fracture permeability under stress was significantly greater than what could be attributed to the elastic deformation of contacts alone.

In real rock formations, the flattening effect observed in the simulation on the ductile rock and caused by plastic

deformation of asperities could be further enhanced by shear displacement under stress that may further smooth the fracture faces out by shearing the asperities off. The gouge (pieces of broken rock) produced during such slip may further complicate the picture by blocking the flow in the fracture and thereby reducing the fracture permeability (Lorenz 1999; Smart et al. 2001).

The changes in the aperture distribution as the fracture closes (see the histogram evolution from Fig. 11a–c) are quite similar to the changes observed in experiments by Muralidharan et al., who used CT scans to quantify the development of fracture aperture under normal stress (Muralidharan et al. 2004). In particular, the emergence of the 'fat tail' in the distribution evident in our Fig. 11c (Fig. 15b) was observed in Muralidharan et al.'s experiments.

The effect of irreversible, plastic normal deformation on the fracture aperture is to compress the statistical distribution of the aperture, so that the apertures fall into a narrower range than they do in a virgin fracture (Fig. 15). The statistical distribution of apertures in a fracture that underwent plastic deformation is different than it was before such deformation. The loading of a fractured rock leaves therefore an 'imprint', or 'memory', about the loading that then stays in the fracture. The roughness of the fracture faces thus carries information about the stress history. This is in a way similar to other stress-memory effects in rocks, such as the Kaiser effect in acoustic emission, a phenomenon well known in rock mechanics (Becker et al. 2010; Lavrov 2003).

Fracture permeability is often anisotropic. For instance, anisotropy can be created by shear displacement (slip) of the fracture faces (Detwiler and Morris 2014). Our simulations show that normal loading is likely to increase the anisotropy of the fracture permeability. This confirms the earlier results of Detwiler and Morris obtained with a much simpler fracture deformation model (Detwiler and Morris 2014).

It should be noted that properties of the rock were identical in the entire rock block in this study. In reality, fracture surfaces can be weathered or damaged, making the strength and stiffness of asperities different from the properties of the bulk material. Incorporating such alterations into the finite-element model of fracture deformation should be trivial, but would require information about the distribution of, for example, cohesion and internal friction angle in the rock, in the direction normal to the fracture face. Such information could be obtained, for example, by a hardness test or a scratch test that enable the estimation of rock properties at different depths from the free surface.

In order to use the proposed computational approach, a validation against experiments is needed. Calibration and validation of the model against experiments for specific rocks is an outstanding task. In order to perform such a

calibration properly, a larger fracture model would need to be used.

Conclusions

A computational framework for evaluating the fracture permeability under normal stress has been developed and tested on two examples: a perfectly elastic ('brittle') rock and an elastic perfectly plastic ('ductile') rock. The two types of rock exhibit significantly different behaviour of fracture permeability under repeated loading. Both mechanical and hydraulic behaviours of the fracture under cyclic normal loading are found to be in qualitative agreement with the results obtained in a number of published experimental studies. The computational approach provides an insight into the actual mechanics of the fracture deformation under stress, and the effect of the latter on the permeability. In particular, a hysteresis in the fracture roughness is obtained with the 'ductile rock', suggesting that (at least some) fractured rocks may have 'memory' about their loading history imprinted in the fracture landscapes. The anisotropy of fracture permeability is reduced as the fracture opens and is increased as the normal stress increases. During repeated loading/unloading of a fracture in a ductile rock, asperities are smoothed out. Therefore, repeated loading/unloading cycles reduce the flow tortuosity and the anisotropy of the fracture permeability. The effect of repeated loading of a ductile rock is also to compress the statistical distribution of the local fracture apertures.

References

Aguilera R (1980) Naturally fractured reservoirs. The Petroleum Publishing Company, Tulsa

Aybar U, Eshkalak MO, Sepehrnoori K, Patzek TW (2014) The effect of natural fracture's closure on long-term gas production from unconventional resources. J Nat Gas Sci Eng 21:1205–1213. doi:10.1016/j.jngse.2014.09.030

Barton N, Bandis S, Bakhtar K (1985) Strength, deformation and conductivity coupling of rock joints. Int J Rock Mech Min Sci Geomech Abstr 22:121–140. doi:10.1016/0148-9062(85)93227-9

Bauget F, Fourar M (2008) Non-Fickian dispersion in a single fracture. J Contam Hydrol 100:137–148. doi:10.1016/j.jconhyd.2008.06.005

Becker D, Cailleau B, Dahm T, Shapiro S, Kaiser D (2010) Stress triggering and stress memory observed from acoustic emission records in a salt mine. Geophys J Int 182:933–948. doi:10.1111/j.1365-246X.2010.04642.x

Brown SR (1987) Fluid flow through rock joints: the effect of surface roughness. J Geophys Res B 92:1337–1347

Brown SR, Scholz CH (1986) Closure of rock joints. J Geophys Res Solid Earth 91:4939–4948. doi:10.1029/JB091iB05p04939

Chen Z, Narayan SP, Yang Z, Rahman SS (2000) An experimental investigation of hydraulic behaviour of fractures and joints in granitic rock. Int J Rock Mech Min Sci 37:1061–1071. doi:10.1016/S1365-1609(00)00039-3

Cumbie DH, McKay LD (1999) Influence of diameter on particle transport in a fractured shale saprolite. J Contam Hydrol 37:139–157. doi:10.1016/S0169-7722(98)00156-9

Cuss RJ, Milodowski A, Harrington JF (2011) Fracture transmissivity as a function of normal and shear stress: first results in Opalinus Clay. Phys Chem Earth A/B/C 36:1960–1971. doi:10.1016/j.pce.2011.07.080

Detwiler RL, Morris JP (2014) Transmissivity anisotropy in rough-walled fractures: the combined influence of shear offset and normal deformation. Paper ARMA 14-7539 presented at the 48th US Rock Mechanics/Geomechanics Symposium held in Minneapolis, MN, USA, 1-4 June 2014

Fournier A, Fussell D, Carpenter L (1982) Computer rendering of stochastic models. Commun ACM 25:371–384. doi:10.1145/358523.358553

Gangi AF (1978) Variation of whole and fractured porous rock permeability with confining pressure. Int J Rock Mech Min Sci Geomech Abstr 15:249–257. doi:10.1016/0148-9062(78)90957-9

Gutierrez M, Øino LE, Nygård R (2000) Stress-dependent permeability of a de-mineralised fracture in shale. Mar Pet Geol 17:895–907. doi:10.1016/S0264-8172(00)00027-1

Keller AA, Roberts PV, Blunt MJ (1999) Effect of fracture aperture variations on the dispersion of contaminants. Water Resour Res 35:55–63. doi:10.1029/1998wr900041

Koyama T, Li B, Jiang Y, Jing L (2008) Numerical simulations for the effects of normal loading on particle transport in rock fractures during shear. Int J Rock Mech Min Sci 45:1403–1419. doi:10.1016/j.ijrmms.2008.01.018

Lavrov A (2003) The Kaiser effect in rocks: principles and stress estimation techniques. Int J Rock Mech Min Sci 40:151–171. doi:10.1016/S1365-1609(02)00138-7

Lavrov A (2005) Fracture-induced physical phenomena and memory effects in rocks: a review. Strain 41:135–149. doi:10.1111/j.1475-1305.2005.00233.x

Lavrov A (2014) Radial flow of non-Newtonian power-law fluid in a rough-walled fracture: effect of fluid rheology. Transp Porous Med 105:559–570. doi:10.1007/s11242-014-0384-6

Lespinasse M, Sausse J (2000) Quantification of fluid flow: hydro-mechanical behaviour of different natural rough fractures. J Geochem Explor 69–70:483–486. doi:10.1016/S0375-6742(00)00111-4

Lorenz JC (1999) Stress-sensitive reservoirs. J Pet Technol 51:61–63

Malama B, Kulatilake PHSW (2003) Models for normal fracture deformation under compressive loading. Int J Rock Mech Min Sci 40:893–901. doi:10.1016/S1365-1609(03)00071-6

MŁynarczuk M (2010) Description and classification of rock surfaces by means of laser profilometry and mathematical morphology

International. J Rock Mech Min Sci 47:138–149. doi:10.1016/j.ijrmms.2009.09.004

Muralidharan V, Chakravarthy D, Putra E, Schechter DS (2004) Investigating fracture aperture distributions under various stress conditions using X-ray CT scanner. Paper 2004-230 presented at the Petroleum Society's 5th Canadian International Petroleum Conference (55th Annual Technical Meeting), Calgary, Alberta, Canada, June 8–10, 2004

Nowamooz A, Radilla G, Fourar M, Berkowitz B (2013) Non-Fickian transport in transparent replicas of rough-walled rock fractures. Transp Porous Med 98:651–682. doi:10.1007/s11242-013-0165-7

Pyrak-Nolte LJ, Morris JP (2000) Single fractures under normal stress: the relation between fracture specific stiffness and fluid flow. Int J Rock Mech Min Sci 37:245–262. doi:10.1016/S1365-1609(99)00104-5

Schmittbuhl J, Steyer A, Jouniaux L, Toussaint R (2008) Fracture morphology and viscous transport. Int J Rock Mech Min Sci 45:422–430. doi:10.1016/j.ijrmms.2007.07.007

Scholz CH, Hickman SH (1983) Hysteresis in the closure of a nominally flat crack. J Geophys Res Solid Earth 88:6501–6504. doi:10.1029/JB088iB08p06501

Smart BGD, Somerville JM, Edlman K, Jones C (2001) Stress sensitivity of fractured reservoirs. J Petrol Sci Eng 29:29–37. doi:10.1016/S0920-4105(00)00088-7

Twiss RJ, Moores EM (2007) Structural geology, 2nd edn. W.H.Freeman, San Francisco

Walsh SDC, Du Frane WL, Sholokhova Y, Settgast R, Johnson SM, Carroll SA (2012) Chemo-mechanical permeability evolution in wellbore-cement fractures exposed to carbon-dioxide-rich brines. Paper ARMA 12-426. Paper presented at the 46th US Rock Mechanics/Geomechanics Symposium held in Chicago, IL, USA, 24–27 June 2012,

Zimmerman RW, Kumar S, Bodvarsson GS (1991) Lubrication theory analysis of the permeability of rough-walled fractures International. J Rock Mech Min Sci Geomech Abstr 28:325–331. doi:10.1016/0148-9062(91)90597-F